

Ultrahigh-energy photons up to 1.4 petaelectronvolts from 12 γ -ray Galactic sources

<https://doi.org/10.1038/s41586-021-03498-z>

Received: 21 October 2020

Accepted: 26 March 2021

Published online: 17 May 2021

 Check for updates

A list of authors and affiliations appears at the end of the paper.

The extension of the cosmic-ray spectrum beyond 1 petaelectronvolt (PeV; 10^{15} electronvolts) indicates the existence of the so-called PeVatrons—cosmic-ray factories that accelerate particles to PeV energies. We need to locate and identify such objects to find the origin of Galactic cosmic rays¹. The principal signature of both electron and proton PeVatrons is ultrahigh-energy (exceeding 100 TeV) γ radiation. Evidence of the presence of a proton PeVatron has been found in the Galactic Centre, according to the detection of a hard-spectrum radiation extending to 0.04 PeV (ref. ²). Although γ -rays with energies slightly higher than 0.1 PeV have been reported from a few objects in the Galactic plane^{3–6}, unbiased identification and in-depth exploration of PeVatrons requires detection of γ -rays with energies well above 0.1 PeV. Here we report the detection of more than 530 photons at energies above 100 teraelectronvolts and up to 1.4 PeV from 12 ultrahigh-energy γ -ray sources with a statistical significance greater than seven standard deviations. Despite having several potential counterparts in their proximity, including pulsar wind nebulae, supernova remnants and star-forming regions, the PeVatrons responsible for the ultrahigh-energy γ -rays have not yet been firmly localized and identified (except for the Crab Nebula), leaving open the origin of these extreme accelerators.

LHAASO is a dual-task facility designed for cosmic-ray (CR) and γ -ray studies at teraelectronvolt and petaelectronvolt energies. It consists of three interconnected detectors—the Water Cherenkov Detector Array (WCDA), Kilometer Square Array (KM2A) and Wide Field-of-view Cherenkov Telescope Array (WFCTA)—located at 4,410 m above sea level in Sichuan Province, China⁷ (see Extended Data Fig. 1).

Detailed studies of the performance of KM2A have been carried out by Monte Carlo simulations, as well as dedicated measurements using the Crab Nebula as a standard candle⁸. At energies above 100 TeV, underground detectors of the deeply penetrating μ mesons provide excellent rejection power (as good as 10^{-5} at 1 PeV) of the background contributed by CR-induced (hadronic) showers. The vast area of the surface detectors of the electromagnetic component of air showers, coupled with the high γ –proton (p) separation efficiency, results in a sensitivity of the full array—in terms of the minimum detectable energy flux ($E^2 dN/dE$, where E is the particle energy and N is the number of particles)—that approaches 10^{-14} erg cm^{-2} s^{-1} , which is substantially below the flux sensitivities of other current and planned space-borne and ground-based γ -ray detectors. At 100 TeV, the angular and energy resolutions are about 15–20 arcmin and better than 20%, respectively, allowing adequate spectroscopic and morphological studies. The detection of γ -rays from an ultrahigh-energy (UHE) source of Crab Nebula strength (energy flux at 100 TeV of $E^2 dN/dE \approx 10^{-12}$ erg cm^{-2} s^{-1}) proceeds in the background-free regime with a rate of 0.1 photon per hour, which exceeds the detection rate of CR-induced showers (after the so-called ‘muon cuts’) by more than an order of magnitude, even for extended, 1° -sized γ -ray emitters⁸.

The analysis of showers detected within a large field of view by the partly completed KM2A in less than one year of operation has revealed

many hot spots as clusters of γ -rays in specific directions of the sky. While the study of the serendipitous search for γ -ray sources is underway, here we report 12 γ -ray sources with energies ≥ 100 TeV detected with statistical significance $\geq 7\sigma$ (see Table 1). From two of them, γ -rays with energy exceeding 0.8 PeV were detected, and the energy of the most energetic photon detected by LHAASO J2032+4102 is 1.4 PeV.

The first source in the list of reported ≥ 100 -TeV sources is the Crab Nebula. An energy spectrum approaching 1 PeV provides the first model-independent evidence that the Crab Nebula operates as an electron PeVatron. In KM2A, Crab is detected as a point-like source. The majority of remaining sources represent diffuse γ -ray structures with angular extensions up to 1° , and all of them are located along the Galactic plane (see Extended Data Fig. 4). At 100 TeV, their fluxes vary from 0.4 to 4 CU (CU, flux of the Crab Nebula at 100 TeV; 1 CU = 6.1×10^{-17} photons TeV^{-1} cm^{-2} s^{-1}). In terms of the distance d , the linear size and γ -ray luminosity of the sources at 100 TeV are $l = 17.5 \frac{\theta}{1^\circ} \frac{d}{(1 \text{ kpc})}$ pc and $L_{\text{UHE}} \approx 10^{32} \left(\frac{d}{1 \text{ kpc}} \right)^2$ CU erg s^{-1} , respectively, where θ is the angular size of the emitter.

Figure 1 shows the spectral energy distributions of three luminous sources with fluxes exceeding 1 CU (at 100 TeV): LHAASO J1825–1326, LHAASO J1908+0621 and LHAASO J2226+6057. Above 100 TeV, the spectra of these sources are steep, characterized by a power-law photon index of $\Gamma \approx 3$. However, a closer look reveals that between 10 TeV and 500 TeV, the spectra experience gradual steepening with energy. To explore this tendency, the spectra were fitted by the so-called log-parabola function $dN/dE \propto E^{-\Gamma(E)}$, where the local photon index $\Gamma(E) = a + b \log E$ (a and b are free parameters) characterizes

Table 1 | UHE γ -ray sources

Source name	RA (°)	dec. (°)	Significance above 100 TeV ($\times\sigma$)	E_{\max} (PeV)	Flux at 100 TeV (CU)
LHAASO J0534+2202	83.55	22.05	17.8	0.88 ± 0.11	1.00(0.14)
LHAASO J1825-1326	276.45	-13.45	16.4	0.42 ± 0.16	3.57(0.52)
LHAASO J1839-0545	279.95	-5.75	7.7	0.21 ± 0.05	0.70(0.18)
LHAASO J1843-0338	280.75	-3.65	8.5	$0.26 - 0.10^{+0.16}$	0.73(0.17)
LHAASO J1849-0003	282.35	-0.05	10.4	0.35 ± 0.07	0.74(0.15)
LHAASO J1908+0621	287.05	6.35	17.2	0.44 ± 0.05	1.36(0.18)
LHAASO J1929+1745	292.25	17.75	7.4	$0.71 - 0.07^{+0.16}$	0.38(0.09)
LHAASO J1956+2845	299.05	28.75	7.4	0.42 ± 0.03	0.41(0.09)
LHAASO J2018+3651	304.75	36.85	10.4	0.27 ± 0.02	0.50(0.10)
LHAASO J2032+4102	308.05	41.05	10.5	1.42 ± 0.13	0.54(0.10)
LHAASO J2108+5157	317.15	51.95	8.3	0.43 ± 0.05	0.38(0.09)
LHAASO J2226+6057	336.75	60.95	13.6	0.57 ± 0.19	1.05(0.16)

Celestial coordinates (RA, dec.); statistical significance of detection above 100 TeV (calculated using a point-like template for the Crab Nebula and LHAASO J2108+5157 and 0.3° extension templates for the other sources); the corresponding differential photon fluxes at 100 TeV; and detected highest photon energies. Errors are estimated as the boundary values of the area that contains $\pm 34.14\%$ of events with respect to the most probable value of the event distribution. In most cases, the distribution is a Gaussian and the error is 1 σ .

the slope of the tangent. For all three spectra, the log-parabola fits are preferred over simple power-law fits. The gradual steepening of multi-hundred-teraelectronvolt γ -rays is partly due to the γ - γ absorption that occurs during their interactions with the diffuse far-infrared and microwave radiation fields. However, as follows from Fig. 1, for all sources the effect of absorption appears to be small, even at the highest energies. These results demonstrate the capability of KM2A for spectral measurements of sharply declining γ -ray fluxes. This achievement is the result of the combination of: (i) a 1-km² detection area providing adequate UHE photon statistics; (ii) suppression of the CR background at the level of 10^{-5} , enabling background-free detection of γ -rays; and (iii) an energy resolution of $<20\%$ constraining the spillover that mainly occurs in the neighbouring energy channels with a width of $\Delta(\log E) = 0.2$.

In Fig. 1, we show also the significance maps of γ -rays with $E \geq 25$ TeV. The two-dimensional images of these sources extend to at least 1°, implying that γ -ray emitters occupy huge ($\geq 10^4$ pc³) regions in the Galactic plane. Although γ -ray emission itself indicates the presence of active or recent particle accelerators inside or in the proximity of γ -ray-emitting regions, the localization and identification of particle accelerators is not a trivial task and requires deep theoretical and phenomenological studies based on comprehensive multi-wavelength data.

Not surprisingly, in the vicinity of the extended UHE sources, one can find potential counterparts for both the γ -ray production regions and the nearby particle accelerators (see Extended Data Table 2). The list includes candidates that are potentially responsible for the electron and proton PeVatrons in the Milky Way: pulsars and pulsar wind nebulae, supernova remnants and young massive star clusters. Detailed studies of the spectral and morphological features of UHE sources and their astrophysical implications are beyond the scope of this paper. The results of in-depth studies of individual LHAASO sources, including the data from both WCDA and KM2A, acquired over three decades from 1 TeV to 1 PeV, will be published elsewhere. Here we limit the discussion to a few general comments on the origin of the UHE radiation.

The only firmly identified source in Table 1 is the Crab Nebula, a representative of pulsar wind nebulae, one of the largest nonthermal source populations in our Galaxy. The Crab Nebula is a peculiar pulsar wind nebula. It differs from other members of this source population by the Crab pulsar's huge spin-down luminosity, $L_0 \approx 5 \times 10^{38}$ erg s⁻¹, compact size (a few parsecs) and large nebular magnetic field, $B \approx 100$ μ G. The latter makes the conversion of the energy of relativistic electrons to inverse Compton γ -rays inefficient, as low as 0.01%. Yet, thanks to the

large spin-down luminosity, the Crab Nebula is a luminous γ -ray source. The rotational powers of other pulsars are smaller by orders of magnitude. On the other hand, the magnetic field strength in the surrounding nebulae is typically smaller than 10 μ G. This dramatically enhances the γ -ray production efficiency, which scales as B^{-2} , and thus compensates for the relatively modest rotational power of pulsars. On the basis of such arguments, pulsar wind nebulae have been predicted, and later established, as a prolific teraelectronvolt γ -ray source population⁹.

The size of a pulsar wind nebula is determined by the region in which electrons, being accelerated at the termination shock, advect with the nebular flow. Typically, it varies between a few to 10 parsecs. These hydrodynamical (usually asymmetric) formations are enveloped by larger and more regular structures consisting of relativistic electrons and positrons that have already left the nebula and propagate diffusively in the interstellar medium⁹. The spectrum and energy-dependent morphology of γ -rays depend on the character of propagation of electrons^{10,11}; therefore, it can be used to measure the diffusion coefficient in the interstellar medium^{9,12}. It has been argued^{13,14} that a considerable fraction of the extended multi-teraelectronvolt γ -ray sources detected by HAWC are linked to these giant 'halos'. This could be also the case for some of the LHAASO sources that presumably host energetic pulsars (see Extended Data Table 2).

A possible realization of this scenario is demonstrated in Extended Data Fig. 5 for LHAASO J1908+0621. It is assumed that electrons are injected with a rate that closely follows the time history of the spin-down luminosity of the pulsar PSR J1907+0602, receiving a constant 6% of the spin-down power. The γ -ray spectral points with energies from giga-electronvolt to several hundred teraelectronvolts could be explained by a power-law spectrum of accelerated electrons with index $\alpha_e = 1.75$, and a super-exponential cutoff at $E_0 = 0.8$ PeV (see Methods). Although acceleration at the wind termination shock could, in principle, boost the energy of electrons to 1 PeV, their escape from the acceleration site and further propagation over distances of tens of parsecs is a challenge. Alternatively, UHE γ -rays can be explained by interactions of protons with the ambient gas through the production and decay of π^0 mesons. If the reported fluxes at giga-electronvolt and teraelectronvolt energies are linked to the UHE source, it is difficult to fit the spectral points in the entire giga-electronvolt–petaelectronvolt energy range of γ -rays using, for example, a simple power law with an exponential cutoff or broken-power-law proton spectra. However, a more complex spectral distribution—for example, a broken power law with an exponential cutoff—can fit the data (see Methods and Extended Data Fig. 5). The production of hadronic UHE γ -rays can

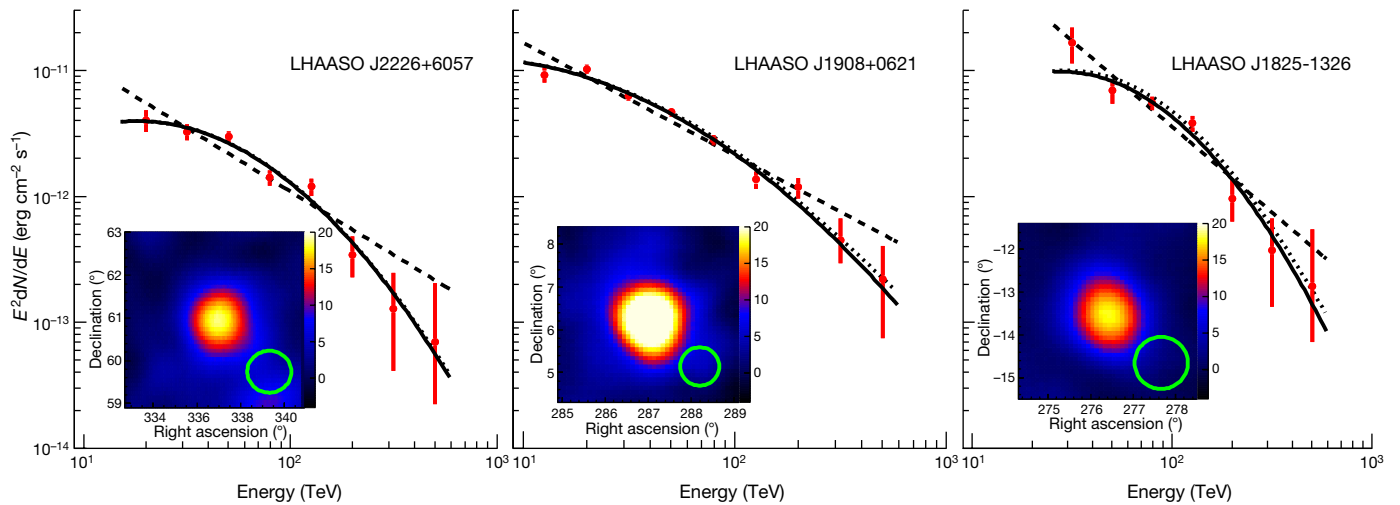


Fig. 1 | Spectral energy distributions and significance maps. **a–c**, Data are shown for LHAASO J2226+6057 (**a**), LHAASO J1908+0621 (**b**), and LHAASO J1825-1326 (**c**). Spectral fits with a log-parabola function (solid lines) in the form of $[E/(10 \text{ TeV})]^{-a-b \log[E/(10 \text{ TeV})]}$ are compared with the power-law fits $E^{-\Gamma}$ for: $a = 1.56$, $b = 0.88$ and $\Gamma = 3.01$ (**a**); $a = 2.27$, $b = 0.46$ and $\Gamma = 2.89$ (**b**); and $a = 0.92$, $b = 1.19$ and $\Gamma = 3.36$ (**c**). The dotted curves correspond to the log-parabola fits corrected for the interstellar γ - γ absorption (see Methods for the radiation fields and Extended Data Fig. 6 for the opacity curves). The comparison of the power-law (PL) model and the log-parabola (LOG) model with the Akaike Information Criterion²⁰ (AIC) gives: $\text{AIC}_{\text{LOG}} = 12.3$ and $\text{AIC}_{\text{PL}} = 24.4$ for LHAASO J2226+6057; $\text{AIC}_{\text{LOG}} = 15.1$ and $\text{AIC}_{\text{PL}} = 30.1$ for LHAASO J1908+0621; and

$\text{AIC}_{\text{LOG}} = 11.6$ and $\text{AIC}_{\text{PL}} = 14.8$ for LHAASO J1825-1326. The insets show the significance maps of the three sources, obtained for γ -rays above 25 TeV. The colour bars show the square root of test statistics (TS), which is equivalent to the significance. The significance ($\sqrt{\text{TS}}$) maps are smoothed with the Gaussian-type point spread function (PSF) of each source. The size of PSFs (68% contamination regions) are shown at the bottom right of each map. We note that the PSFs of the three sources are slightly different owing to different inclination angles. Namely, the 68% contamination angles are 0.49° for LHAASO J2226+6057, 0.45° for LHAASO J1908+0621 and 0.62° for LHAASO J1825-1326. Error bars represent one standard deviation.

be realized in a scenario in which the accelerated particles have left their acceleration site (for example, a supernova remnant) and have entered nearby high-density clouds¹⁵. The energy spectrum of protons approaching the clouds depends not only on the initial (acceleration) spectrum but also on the propagation (energy-dependent) timescales of CRs and on the distances to the clouds. Therefore, one may indeed expect unusual energy distributions of CRs inside the clouds¹⁶. In this scenario, the middle-aged supernova remnant SNR G40.5-0.5, overlapping with the image of LHAASO J1908+0621, could play the role of the particle accelerator. It is too old to be a multi-teraelectronvolt γ -ray emitter itself, but CR protons and nuclei accelerated at the early epochs of this supernova remnant can initiate high-energy emission in the surrounding clouds. If confirmed, this would be the first strong evidence of acceleration of petaelectronvolt protons by an supernova remnant.

Although supernova remnants remain prime candidates as suppliers of Galactic CRs, massive stars with powerful winds have been proposed as a viable alternative to supernova remnants^{17,18}, primarily as contributors to the ‘knee’ region around 1 PeV. A preference for young massive star clusters as proton PeVatrons over supernova remnants has recently been argued in the context of the $1/r$ -type (where r is the distance from the cluster) spatial distributions of parent protons, derived from the observations of extended teraelectronvolt γ -ray sources associated with luminous stellar clusters, in particular with Cygnus OB2¹⁹. The positional coincidence of LHAASO J2032+4102 with the Cygnus Cocoon that surrounds Cygnus OB2, and with photons exceeding 1 PeV emitted from it, can be treated as evidence of the operation of massive stars as hadronic PeVatrons. The leptonic (inverse Compton) origin of radiation can be excluded because of the lack of brightening of the γ -ray image towards Cygnus OB2. A decisive test for the acceleration of protons, presumably via collisions of the stellar winds, and continuous injection into the circumstellar medium over million-year timescales, would be the derivation of hard injection spectra and a radial dependence of the density of UHE protons. Adequate photon statistics provided by LHAASO for spectrometric

and morphological studies of this object, which is located in a rather complex region crowded by several competing sources, is foreseen for the coming 1–2 years.

Regardless of the nature of objects associated with the UHE sources, the photons detected by LHAASO far beyond 100 TeV prove the existence of Galactic PeVatrons. Moreover, it is likely that the Milky Way is full of these perfectly designed particle accelerators. The acceleration of protons to petaelectronvolt energies requires extreme physical conditions, representing a challenge for any Galactic source population, including supernova remnants and young massive star clusters, as suspected major contributors to Galactic CRs. Pulsar wind nebulae as potential (in fact, the only feasible) electron PeVatrons in our Galaxy require even more extreme theoretical speculations. The 12 UHE sources reported here, detected at about 1 CU, reveal only the tip of the iceberg. In the coming years, observations with LHAASO will reduce the flux detection threshold by at least an order of magnitude. This will dramatically increase the number of UHE sources and, at the same time, provide high-quality energy spectra and the morphology of UHE sources in the flux range of 1 CU. Extension of the spectra without an indication of a cutoff beyond several petaelectronvolts would not only robustly identify the hadronic origin of the UHE γ radiation but, more importantly, would reveal the sites of super-PeVatrons, the CR factories in the Milky Way responsible for the locally observed flux of CRs well above the ‘knee’.

Online content

Any methods, additional references, Nature Research reporting summaries, source data, extended data, supplementary information, acknowledgements, peer review information; details of author contributions and competing interests; and statements of data and code availability are available at <https://doi.org/10.1038/s41586-021-03498-z>.

1. Aloisio, R., Cocchia, E. & Vissani, F. (eds) *Multiple Messengers and Challenges in Astroparticle Physics* (Springer, 2018).

2. HESS Collaboration. Acceleration of petaelectronvolt protons in the Galactic Centre. *Nature* **531**, 476–479 (2016).
3. Amenomori, M. et al. First detection of photons with energy beyond 100 TeV from an astrophysical source. *Phys. Rev. Lett.* **123**, 051101 (2019).
4. Abeysekara, A. U. et al. Multiple Galactic sources with emission above 56 TeV detected by HAWC. *Phys. Rev. Lett.* **124**, 021102 (2020).
5. Abeysekara, A. U. et al. HAWC observations of the acceleration of very-high-energy cosmic rays in the Cygnus Cocoon. *Nat. Astron.* <https://doi.org/10.1038/s41550-021-01318-y> (2021).
6. Amenomori, M. et al. Potential PeVatron supernova remnant G106.3+2.7 seen in the highest-energy gamma rays. *Nat. Astron.* <https://doi.org/10.1038/s41550-020-01294-9> (2021).
7. Cao, Z. A future project at Tibet: the large high altitude air shower observatory (LHAASO). *Chin. Phys. C* **34**, 249–252 (2010).
8. Aharonian, F. et al. Observation of the Crab Nebula with LHAASO-KM2A – a performance study. *Chin. Phys. C* **45**, 025002 (2021).
9. Aharonian, F. A. *Very High Energy Cosmic Gamma Radiation: A Crucial Window on the Extreme Universe* (World Scientific, 2004).
10. Liu, R.-Y. & Yan, H. On the unusually large spatial extent of the TeV nebula HESS J1825–137: implication from the energy-dependent morphology. *Mon. Not. R. Astron. Soc.* **494**, 2618–2627 (2020).
11. Giacinti, G., et al. Halo fraction in TeV-bright pulsar wind nebulae. *Astron. Astrophys.* **636**, A113 (2020).
12. Abeysekara, A. U. et al. Extended gamma-ray sources around pulsars constrain the origin of the positron flux at Earth. *Science* **358**, 911–914 (2017).
13. Linden, T. et al. Using HAWC to discover invisible pulsars. *Phys. Rev. D* **96**, 103016 (2017).
14. Sudoh, T., Linden, T. & Beacom, J. F. TeV halos are everywhere: prospects for new discoveries. *Phys. Rev. D* **100**, 043016 (2019).
15. Gabici, S. & Aharonian, F. A. Searching for Galactic cosmic-ray pevatrons with multi-TeV gamma rays and neutrinos. *Astrophys. J. Lett.* **665**, L131–L134 (2007).
16. Aharonian, F. A. & Atayan, A. M. On the emissivity of π^0 -decay gamma radiation in the vicinity of accelerators of Galactic cosmic rays. *Astron. Astrophys.* **309**, 917–928 (1996).
17. Cesarsky, C. J. & Montmerle, T. Gamma-rays from active regions in the Galaxy – the possible contribution of stellar winds. *Space Sci. Rev.* **36**, 173–193 (1983).
18. Bykov, A. M. et al. High-energy particles and radiation in star-forming regions. *Space Sci. Rev.* **216**, 42 (2020).
19. Aharonian, F., Yang, R. & de Oña Wilhelmi, E. Massive stars as major factories of Galactic cosmic rays. *Nat. Astron.* **3**, 561–567 (2019).
20. Akaike, H. A new look at the statistical model identification. *IEEE Trans. Automat. Contr.* **19**, 716C723 (1974)

Publisher's note Springer Nature remains neutral with regard to jurisdictional claims in published maps and institutional affiliations.

© The Author(s), under exclusive licence to Springer Nature Limited 2021

Zhen Cao^{1,2,3,4,5,6,7,8,9,10,11,12,13,14,15,16,17,18,19,20,21,22,23,24,25,26,27,28,29,30,31,32,33,34,35,36,37,38,39,40,41,42,43,44,45,46,47,48,49,50,51,52,53,54,55,56,57,58,59,60,61,62,63,64,65,66,67,68,69,70,71,72,73,74,75,76,77,78,79,80,81,82,83,84,85,86,87,88,89,90,91,92,93,94,95,96,97,98,99,100,101,102,103,104,105,106,107,108,109,110,111,112,113,114,115,116,117,118,119,120,121,122,123,124,125,126,127,128,129,130,131,132,133,134,135,136,137,138,139,140,141,142,143,144,145,146,147,148,149,150,151,152,153,154,155,156,157,158,159,160,161,162,163,164,165,166,167,168,169,170,171,172,173,174,175,176,177,178,179,180,181,182,183,184,185,186,187,188,189,190,191,192,193,194,195,196,197,198,199,200,201,202,203,204,205,206,207,208,209,210,211,212,213,214,215,216,217,218,219,220,221,222,223,224,225,226,227,228,229,230,231,232,233,234,235,236,237,238,239,240,241,242,243,244,245,246,247,248,249,250,251,252,253,254,255,256,257,258,259,260,261,262,263,264,265,266,267,268,269,270,271,272,273,274,275,276,277,278,279,280,281,282,283,284,285,286,287,288,289,290,291,292,293,294,295,296,297,298,299,300,301,302,303,304,305,306,307,308,309,310,311,312,313,314,315,316,317,318,319,320,321,322,323,324,325,326,327,328,329,330,331,332,333,334,335,336,337,338,339,340,341,342,343,344,345,346,347,348,349,350,351,352,353,354,355,356,357,358,359,360,361,362,363,364,365,366,367,368,369,370,371,372,373,374,375,376,377,378,379,380,381,382,383,384,385,386,387,388,389,390,391,392,393,394,395,396,397,398,399,400,401,402,403,404,405,406,407,408,409,410,411,412,413,414,415,416,417,418,419,420,421,422,423,424,425,426,427,428,429,430,431,432,433,434,435,436,437,438,439,440,441,442,443,444,445,446,447,448,449,450,451,452,453,454,455,456,457,458,459,460,461,462,463,464,465,466,467,468,469,470,471,472,473,474,475,476,477,478,479,480,481,482,483,484,485,486,487,488,489,490,491,492,493,494,495,496,497,498,499,500,501,502,503,504,505,506,507,508,509,510,511,512,513,514,515,516,517,518,519,520,521,522,523,524,525,526,527,528,529,530,531,532,533,534,535,536,537,538,539,540,541,542,543,544,545,546,547,548,549,550,551,552,553,554,555,556,557,558,559,560,561,562,563,564,565,566,567,568,569,570,571,572,573,574,575,576,577,578,579,580,581,582,583,584,585,586,587,588,589,590,591,592,593,594,595,596,597,598,599,600,601,602,603,604,605,606,607,608,609,610,611,612,613,614,615,616,617,618,619,620,621,622,623,624,625,626,627,628,629,630,631,632,633,634,635,636,637,638,639,640,641,642,643,644,645,646,647,648,649,650,651,652,653,654,655,656,657,658,659,660,661,662,663,664,665,666,667,668,669,670,671,672,673,674,675,676,677,678,679,680,681,682,683,684,685,686,687,688,689,690,691,692,693,694,695,696,697,698,699,700,701,702,703,704,705,706,707,708,709,710,711,712,713,714,715,716,717,718,719,720,721,722,723,724,725,726,727,728,729,730,731,732,733,734,735,736,737,738,739,740,741,742,743,744,745,746,747,748,749,750,751,752,753,754,755,756,757,758,759,760,761,762,763,764,765,766,767,768,769,770,771,772,773,774,775,776,777,778,779,780,781,782,783,784,785,786,787,788,789,790,791,792,793,794,795,796,797,798,799,800,801,802,803,804,805,806,807,808,809,810,811,812,813,814,815,816,817,818,819,820,821,822,823,824,825,826,827,828,829,830,831,832,833,834,835,836,837,838,839,840,841,842,843,844,845,846,847,848,849,850,851,852,853,854,855,856,857,858,859,860,861,862,863,864,865,866,867,868,869,870,871,872,873,874,875,876,877,878,879,880,881,882,883,884,885,886,887,888,889,890,891,892,893,894,895,896,897,898,899,900,901,902,903,904,905,906,907,908,909,910,911,912,913,914,915,916,917,918,919,920,921,922,923,924,925,926,927,928,929,930,931,932,933,934,935,936,937,938,939,940,941,942,943,944,945,946,947,948,949,950,951,952,953,954,955,956,957,958,959,960,961,962,963,964,965,966,967,968,969,970,971,972,973,974,975,976,977,978,979,980,981,982,983,984,985,986,987,988,989,990,991,992,993,994,995,996,997,998,999,1000}

Y. F. Liang²⁸, S. J. Lin¹⁶, B. Liu⁷, C. Liu¹², D. Liu²², H. Liu⁸, H. D. Liu²⁴, J. Liu¹², J. L. Liu^{29,30}, J. S. Liu¹⁸, J. Y. Liu¹², M. Y. Liu¹⁶, R. Y. Liu^{10,32}, S. M. Liu¹³, W. Liu¹², Y. N. Liu²³, Z. X. Liu⁹, W. J. Long⁹, R. Lu¹⁹, H. K. Lv¹², B. Q. Ma²⁷, L. L. Ma¹², X. H. Ma¹², J. R. Mao²⁵, A. Masood⁸, W. Mitthumsiri³¹, T. Montaruli²⁰, Y. C. Nan²², B. Y. Pang⁸, P. Pattarakijwanich³¹, Z. Y. Pei¹¹, M. Y. Qi¹², D. Ruffolo³¹, V. Rubev²⁶, A. Sáiz³¹, L. Shao¹⁴, O. Shchegolev^{26,32}, X. D. Sheng¹², J. R. Shi¹², H. C. Song²⁷, Yu. V. Stenkin^{26,32}, V. Stepanov²⁶, Q. N. Sun⁹, X. N. Sun²⁸, Z. B. Sun³³, P. H. T. Tam¹⁸, Z. B. Tang⁶⁷, W. W. Tian³¹⁷, B. D. Wang¹², C. Wang³³, H. Wang⁸, H. G. Wang¹¹, J. C. Wang²⁵, J. S. Wang^{29,30}, L. P. Wang²², L. Y. Wang¹², R. N. Wang⁸, W. Wang¹⁸, W. Wang¹², X. G. Wang²⁹, X. J. Wang¹², X. Y. Wang¹⁰, Y. D. Wang¹², Y. J. Wang¹², Y. P. Wang^{12,3}, Zheng Wang^{61,2}, Zhen Wang^{29,30}, Z. H. Wang⁹, Z. X. Wang¹⁹, D. M. Wei¹³, J. J. Wei¹³, Y. J. Wei^{12,3}, T. Wen¹⁹, C. Y. Wu¹², H. R. Wu¹², S. Wu¹², W. X. Wu⁸, X. F. Wu¹³, S. Q. Xi⁸, J. Xia⁷¹³, J. J. Xia⁸, G. M. Xiang³¹⁵, G. Xiao¹², H. B. Xiao¹¹, G. G. Xin¹², Y. L. Xin⁸, Y. Xing¹⁵, D. L. Xu^{29,30}, R. X. Xu²⁷, L. Xue²², D. H. Yan²⁵, C. W. Yang⁹, F. F. Yang^{61,2}, J. Y. Yang¹⁸, L. L. Yang¹⁸, M. J. Yang¹², R. Z. Yang^{7,33}, S. B. Yang¹⁹, Y. H. Yao⁹, Z. G. Yao¹², Y. M. Ye²³, L. Q. Yin¹², N. Yin²², X. H. You¹², Z. Y. You^{12,3}, Y. H. Yu²², Q. Yuan¹³, H. D. Zeng¹³, T. X. Zeng^{61,2}, W. Zeng¹⁹, Z. K. Zeng^{12,3}, M. Zha¹², X. X. Zhai¹², B. B. Zhang¹⁰, H. M. Zhang¹⁰, H. Y. Zhang²², J. L. Zhang¹⁷, J. W. Zhang⁹, L. Zhang¹⁴, Li Zhang¹⁹, L. X. Zhang¹¹, P. F. Zhang¹⁹, P. P. Zhang¹⁴, R. Zhang⁷¹³, S. R. Zhang¹⁴, S. S. Zhang¹², X. Zhang¹⁰, X. P. Zhang¹², Yong Zhang¹², Yi Zhang^{11,3}, Y. F. Zhang⁸, Y. L. Zhang¹², B. Zhao⁸, J. Zhao¹², L. Zhao⁶⁷, L. Z. Zhao¹⁴, S. P. Zhao^{13,22}, F. Zheng³³, Y. Zheng⁸, B. Zhou¹², H. Zhou^{29,30}, J. N. Zhou¹⁵, P. Zhou¹⁹, R. Zhou⁹, X. X. Zhou⁸, C. G. Zhu²², F. R. Zhu⁸, H. Zhu¹⁷, K. J. Zhu^{61,2,3} & X. Zuo¹²

¹Key Laboratory of Particle Astrophysics & Experimental Physics Division & Computing Center, Institute of High Energy Physics, Chinese Academy of Sciences, Beijing, China. ²TIANFU Cosmic Ray Research Center, Chengdu, Sichuan, China. ³University of Chinese Academy of Sciences, Beijing, China. ⁴Dublin Institute for Advanced Studies, Dublin, Ireland. ⁵Max-Planck-Institut für Nuclear Physics, Heidelberg, Germany. ⁶State Key Laboratory of Particle Detection and Electronics, Beijing, China. ⁷University of Science and Technology of China, Hefei, China. ⁸School of Physical Science and Technology & School of Information Science and Technology, Southwest Jiaotong University, Chengdu, China. ⁹College of Physics, Sichuan University, Chengdu, China. ¹⁰School of Astronomy and Space Science, Nanjing University, Nanjing, China. ¹¹Center for Astrophysics, Guangzhou University, Guangzhou, China. ¹²School of Physics and Technology, Wuhan University, Wuhan, China. ¹³Key Laboratory of Dark Matter and Space Astronomy, Purple Mountain Observatory, Chinese Academy of Sciences, Nanjing, China. ¹⁴Hebei Normal University, Shijiazhuang, China. ¹⁵Key Laboratory for Research in Galaxies and Cosmology, Shanghai Astronomical Observatory, Chinese Academy of Sciences, Shanghai, China. ¹⁶Key Laboratory of Cosmic Rays (Tibet University), Ministry of Education, Lhasa, Tibet, China. ¹⁷National Astronomical Observatories, Chinese Academy of Sciences, Beijing, China. ¹⁸School of Physics and Astronomy & School of Physics (Guangzhou), Sun Yat-sen University, Zhuhai, China. ¹⁹School of Physics and Astronomy, Yunnan University, Kunming, China. ²⁰Département de Physique Nucléaire et Corpusculaire, Faculté de Sciences, Université de Genève, Geneva, Switzerland. ²¹Dipartimento di Fisica dell'Università di Napoli "Federico II", Complesso Universitario di Monte Sant'Angelo, Naples, Italy. ²²Institute of Frontier and Interdisciplinary Science, Shandong University, Qingdao, China. ²³Department of Engineering Physics, Tsinghua University, Beijing, China. ²⁴School of Physics and Microelectronics, Zhengzhou University, Zhengzhou, China. ²⁵Yunnan Observatories, Chinese Academy of Sciences, Kunming, China. ²⁶Institute for Nuclear Research of Russian Academy of Sciences, Moscow, Russia. ²⁷School of Physics, Peking University, Beijing, China. ²⁸School of Physical Science and Technology, Guangxi University, Nanning, China. ²⁹Tsung-Dao Lee Institute, Shanghai Jiao Tong University, Shanghai, China. ³⁰School of Physics and Astronomy, Shanghai Jiao Tong University, Shanghai, China. ³¹Department of Physics, Faculty of Science, Mahidol University, Bangkok, Thailand. ³²Moscow Institute of Physics and Technology, Moscow, Russia. ³³National Space Science Center, Chinese Academy of Sciences, Beijing, China. ✉e-mail: caozh@ihep.ac.cn; felix.aharonian@mpi-hd.mpg.de; chensz@ihep.ac.cn; ryllu@nju.edu.cn; yangrz@ustc.edu.cn

Methods

The LHAASO experiment

The three major components of LHAASO. The Large High Altitude Air Shower Observatory (LHAASO)⁷ is a complex of extensive air shower (EAS) detector arrays located on Mountain Haizi (29° 21' 27.6" N, 100° 08' 19.6" E), 4,410 m above sea level, in Sichuan, China. It consists of three interconnected detector arrays, KM2A, WCDA and WFCTA, as schematically illustrated in Extended Data Fig. 1.

WCDA²¹ reaches a sensitivity of 9 mCU per year for γ -ray sources of a few teraelectronvolts by using three water ponds of a total area of 78,000 m², filled to a depth of 4.5 m, that fully absorb the air shower particles. The shower arrival direction is measured with an angular resolution of about 0.2° above a few teraelectronvolts. WCDA covers a wide energy interval bridging FERMI-LAT and KM2A by having the same sensitivity of FERMI-LAT and KM2A at 200 GeV and 20 TeV, respectively. As a detector that continuously surveys 1/6 of the sky at any moment, WCDA is a device designed for monitoring and following up any transient phenomenon that may happen in its energy window. WFCTA consists of 18 telescopes designed for detection of atmospheric Cherenkov light produced by secondary particles (mainly electrons and positrons) from air showers initiated by primary CRs with energy ranging from 50 TeV to 100 PeV. The large field of view of the telescopes, 16° × 16° each, allows the telescope array to cover a wide patch of the sky for diffused CR measurements. The combined operation of these telescopes with KM2A and WCDA enables highly desired spectrum measurements of different CR species in a wide energy range that includes the spectral features known as 'first knee' and 'second knee'.

KM2A and its performance. KM2A comprises an array^{7,21} of 5,195 scintillation counters (EDs) deployed on a 15-m grid, and an array of 1,188 undersurface muon detectors (MDs) deployed on a 30-m grid, both covering an area of 1 km², plus a 0.3-km² skirt array used to identify showers falling outside the central area, as illustrated in Extended Data Fig. 1. For a more complete description of the EDs and MDs, the hardware calibration, and the data selection and reconstruction procedure; see ref.⁸. Here, we provide a brief description. The KM2A half-array currently in operation includes 2,365 EDs. Each ED is made of four plastic scintillation tiles (100 cm × 25 cm × 1 cm) covered by a 5-mm-thick lead plate. Embedded wavelength-shifting fibres transfer the scintillation light to a photomultiplier tube (PMT). The charge output is used to measure the number of crossing shower particles with excellent linearity for up to more than 10⁴ particles. The time resolution is about 2 ns. All of the EDs are synchronized within 0.2 ns. The shower trigger logic requires, for the KM2A half-array, at least 20 EDs fired within a window of 400 ns. This trigger allows fully efficient detection of shower events of energy above 10 TeV. The ED signals are used to determine the impact point of the shower axis, the shower size and the arrival direction. Above 60 TeV, the core location is determined with an accuracy better than 3 m, enabling a high-precision measurement of the shower arrival direction with an angular resolution of $\leq 0.3^\circ$ for γ -induced showers of up to 40° zenith angle. This is verified by the observation of well known γ -ray point sources such as the Crab Nebula, as reported elsewhere⁸, and LHAASO J2108+5157 (11th source in Table 1), which has nearly no extension measured.

By reconstructing the shower profile, the particle density evaluated at a distance of 50 m from the shower core is used to estimate the energy of the primary γ -ray. The energy resolution is better than 14% for photons above 100 TeV arriving from a zenith angle of $< 35^\circ$. This defines the bin size of $\Delta(\log E) = 0.2$ in the measurements of the spectral energy distributions (SEDs) of the sources to minimize bin-to-bin migration mainly between adjacent bins. Further examination for any non-Gaussian tails of the energy resolution function—defined as the distribution of $(E_{\text{rec}} - E_{\text{true}})/E_{\text{true}}$, where E_{rec} is the reconstructed photon energy and E_{true} is the thrown-in energy in the shower/detector simulation—is carried out.

The distributions of E_{true} of events that are in each E_{rec} bin are plotted in Extended Data Fig. 2a for all 12 bins in the energy range from 10 TeV to 2.5 PeV. The distribution is defined as the fraction $(dN/dE_{\text{true}})/N_i$, where N_i is total number of events in the i th bin defined by the reconstructed energy E_{rec} . It is found that the non-Gaussian effect is very small. The remaining effect brings some events that have higher true energies to the bin at lower E_{rec} , meaning that the shower energy is underestimated. In the opposite direction, there is no clear overestimation effect due to a non-Gaussian tail. Integrating the fraction in the bin defines the so-called bin purity. The purities in all bins are plotted as a function of energy in Extended Data Fig. 2b. The fraction of 67% around 100 TeV indicates that the bin size matches the energy resolution, as expected. The remaining 33% of events mainly come from the adjacent bins, as described by the Gaussian-like functions in Extended Data Fig. 2a. The increasing trend with energy demonstrates that the spillover effect due to both Gaussian and non-Gaussian features of the resolution function is decreasing with energy. Because the SEDs of γ -ray sources typically follow a very steep power law—for example, with an index of -3.09 for the Crab Nebula⁸—the spillover effect in a wide energy range from 10 TeV to few petaelectronvolts was further examined by the following procedure. Events generated using the Crab Nebula SED but cut at E_{cut} are reconstructed and plotted as the distribution of the number of events in bins defined by E_{rec} . As E_{cut} runs through 20 TeV, 40 TeV, ..., 1.3 PeV and 1.5 PeV, the spillover effect is determined by events in the bins above E_{cut} . As shown in Extended Data Fig. 3, the spillover mainly happens in the adjacent bin, and the fraction of events in the next-adjacent bin is very small. The effect is also reduced with energy. The fraction runs lower than 1% for $E_{\text{cut}} > 400$ TeV even in the adjacent bin. The same tests were applied to J2226+6057 and J1825-1326, the most northern and southern sources in Table 1, respectively, and similar results were found.

The critical part of KM2A is the muon detector (MD) array, consisting of 1,188,36 m² water Cherenkov detectors buried 2.5 m beneath the soil surface. Each tank is filled with pure water 1.2 m in depth. An 8-inch PMT is immersed in the water volume at the roof centre of the tank to collect the Cherenkov light produced by high-energy particles passing through the water. The charge output is used to count the number of particles (muons), with a resolution of $\sigma/n \approx 20\%/\sqrt{n}$. The time resolution is about 10 ns. The electromagnetic component of the shower is shielded by the soil overburden, which corresponds to about 20 radiation lengths, making each MD a very clean detector of > 1 GeV muons. The KM2A half-array consists of 578 MDs uniformly distributed with a total active area of 18,800 m², whose information is used to select γ -ray-induced showers. A shower initiated by a high-energy γ contains fewer muons than a primary CR-induced air shower. Thus, using the ratio N_μ/N_e as a selection criterion (where N_μ is the total number of muons measured by MDs and N_e is the total number of particles counted by EDs), KM2A is capable of rejecting the CR background by a factor of 10^{-2} at 20 TeV and 10^{-4} above 100 TeV. Together with an angular resolution of 0.3° (68% containment angle of flux from a point source), the KM2A half-array is an essentially background-free γ -ray detector at energies > 100 TeV. Quantitatively, the differential sensitivity of the current half-array is sufficient to detect any source with an energy flux greater than 1.8×10^{-13} erg cm⁻² s⁻¹ between 100 TeV and 178 TeV with a significance of 5σ in a year of data taking. A significance of 30σ obtained for the detection of the Crab Nebula in 136 days indicates that an integrated sensitivity of 1.1×10^{-14} erg cm⁻² s⁻¹ was achieved above 25 TeV.

Data taken with KM2A-1/2 and SED measurements for three sources.

The partial configuration of KM2A—a half-array with 2,365 EDs and 578 MDs in stable operation—is detailed in ref.⁸. KM2A has been operating for data taking since 27 December 2019, for a live time of 308.33 days. After data reconstruction, showers with zenith angle $< 50^\circ$ and energy > 100 TeV are selected as γ -like events using the muon content criterion, that is, $N_\mu/N_e < 1/230$. In total, about 84,000 γ -like events are used to survey the sky declination band $-15^\circ < \delta < 75^\circ$ in search for

UHE sources. The sky map in celestial coordinates (right ascension, RA; declination, dec.) is divided into a grid of $0.1^\circ \times 0.1^\circ$ bins, and filled with detected events according to their reconstructed arrival direction (event map). The number of residual CR background events in each bin (background map) is estimated using the direct integration method²², which was developed specifically for measurements with detector arrays^{4,23}. Then the background map is subtracted from the event map, obtaining the source map. A smoothing procedure is applied to take into account the KM2A angular resolution. The significance of the excess of γ -like events in each bin is estimated via a likelihood ratio test between the one-source model (source signals plus background) and the background-only model. Because the angular distribution is clearly wider than the detector angular resolution, an a priori 0.3° intrinsic extension of the sources is assumed as a Gaussian template in the estimation of the significance. Twelve sources of γ -rays are found with signals above 7σ at energies above 100 TeV, as listed in Table 1. The sky map of γ -rays above 100 TeV is shown in Extended Data Fig. 4. The corresponding exposure time and photon statistics for each source are shown in Extended Data Table 1.

Above 400 TeV, KM2A measures γ -rays essentially background-free. Every single photon has its own energy measured independently. The highest-energy (E_{\max}) photons, which define the maximum energy detected for each source, are listed in Table 1. To verify the detection and estimate the uncertainty associated with the measurement of E_{\max} , a large number of photon events are generated using the geometric parameters of the measured events over a wide energy range. For instance, 10,000 events are generated for a 1.4-PeV photon. The distribution of thrown-in energies of events that have a total number of particles recorded by the registered EDs and a number of EDs similar to those of the detected values, within $\pm 10\%$, is used to estimate the photon energy and its error. Thus, the spillover effect due to any non-Gaussian tail is further checked. 10% is quite a large range of the total number of particles (5σ from the measured value) and of the number of EDs (2σ from the measured value). For this highest-energy photon from the Cygnus region, the measured ratio $N_{\mu}/N_e = 1/941$ rejects almost all CR background. The chance probability is estimated to be 0.028% by using 1,044 observed events with reconstructed energy higher than 1.4 PeV in the 1° cone centred at the source location given in Table 1.

For the three most significantly detected sources, LHAASO J1825-1326, LHAASO J1908+0621 and LHAASO J2226+6057, we determine their SEDs. To calculate the photon fluxes correctly, the intrinsic extent of the sources is estimated by quadratically subtracting the width of the point spread function (PSF), measured using the Crab Nebula data, from the measured angular distributions; we find $(0.30 \pm 0.06)^\circ$, $(0.58 \pm 0.04)^\circ$ and $(0.36 \pm 0.06)^\circ$, respectively. Over the entire energy range from 10 TeV to 1 PeV, photon fluxes are calculated in 10 bins of width $\Delta(\log E) = 0.2$ by taking into account the extents. The γ -ray signals and corresponding backgrounds are integrated over the angular range, in which 90% of the probability of the Gaussian template is contained, as the measured signal in each energy bin, respectively. The SEDs are then derived using a forward unfolding procedure based on the least- χ^2 algorithm and are shown in Fig. 1.

Previous measurements of 100-TeV γ -rays. The first attempts to explore the petaelectronvolt γ -ray sky with ground-based CR facilities were made in the 1980s. Despite some exciting but controversial discovery claims, these results have not been confirmed by detectors designed explicitly for γ -ray observations, in particular by CASA-MIA^{24,25}. The latter had adequate ($\sim 1/4$ km²) area of surface detectors, however the density of muon detectors ($\sim 1\%$) was not sufficient for suppression of the background (hadronic) showers at a level better than 10^{-4} , which would allow detection of UHE sources reported in this paper. Recently, the AS γ ³ and HAWC⁴ collaborations, using high-altitude air shower facilities, reported marginal detections of γ -rays above 100 TeV from a few Galactic sources, including the Crab Nebula. Detections of γ -rays

with energy close to 100 TeV have also been reported by the Cherenkov telescope arrays HEGRA²⁶ and MAGIC²⁷. Apart from their scientific value, these results exhibited the need to study the UHE sky at a depth well below the Crab Nebula flux and at energies well beyond 100 TeV. Table 1 demonstrates that LHAASO has achieved these targets. With the fully completed facility, the search for ≥ 100 -TeV sources at the level of 0.1 CU would be a matter of one-year exposure.

Possible counterparts of LHAASO sources. For all twelve sources reported in Table 1, we searched for their possible astrophysical associations and teraelectronvolt counterparts located $<1^\circ$ away from the measured centres, including pulsars and corresponding pulsar wind nebulae, supernova remnants, young massive star clusters and H II regions. The results are listed in Extended Data Table 2.

Relevant background information and multi-wavelength analysis

0.8 γ -ray opacity. The attenuation of high-energy Galactic γ -rays is due to pair production ($\gamma\gamma \rightarrow e^+e^-$) from γ -rays interacting with background photons from both the cosmic microwave background (CMB) and interstellar radiation fields (ISRF). The photon-photon pair production cross-section, averaged over directions of the background radiation field, depends on the product of the energies of colliding photons. For a given energy of γ -ray photons, E_γ , this cross-section peaks at the wavelength of the background photons, $\lambda \approx 1[E_\gamma/(1 \text{ TeV})]^{-1} \mu\text{m}$. Thus, the γ -ray opacity above and below 100 TeV is due to the absorption on CMB and ISRF, respectively. The opacity was calculated by calculating the line-of-sight integral of the product of the pair production cross-section with the energy density of the radiation fields. The dependence of the pair production cross-section on the energy is given in ref.²⁸. The ISRF energy density is taken from ref.²⁹. The general formalism can be found in ref.³⁰. The γ -ray opacities for LHAASO J2226+6057, J1908+0621, J1825-1326 and the Crab Nebula are shown in Extended Data Fig. 6.

Fermi LAT analysis for LHAASO J1908+0621. To estimate the gigaelectronvolt emissions in the region of LHAASO J1908+0621, we analysed Fermi LAT data obtained over 11 years towards this source. For this analysis we selected the Fermi LAT Pass 8 database from 4 August 2008 (MET 239557417) until 17 January 2020 (MET 600946580). A $10^\circ \times 10^\circ$ square region centred at the best-fit position of LHAASO J1908+0621 (RA = 287.18°, dec. = 6.18°) was chosen as the region of interest (ROI). We used the ‘source’ event class, and the recommended data cut expression (DATA_QUAL > 0) && (LAT_CONFIG == 1) to exclude time periods in which spacecraft events affected the data quality. To reduce the background contamination from Earth’s albedo, only the events with zenith angles less than 90° were taken into account in the analysis. Moreover, we used FermiTools from the Conda distribution (<https://github.com/fermi-lat/FermiTools-conda>) together with the latest version of the instrument response functions P8R3_SOURCE_V2. In our background model, we included the sources in the Fermi LAT eight-year catalogue³¹ within the ROI enlarged by 7° . The normalization factors and the spectral indices of all sources within 5° of the ROI centre were set as free parameters. For the diffuse background components, we used the latest Galactic diffuse model gll_iem_v07.fits and the isotropic emission model iso_P8R3_SOURCE_V2_v1.txt (<https://fermi.gsfc.nasa.gov/ssc/data/access/lat/BackgroundModels.html>) with their normalization parameters free. The high-energy γ -ray emission region found in the KM2A data overlaps with the bright pulsar PSR J1907+0602. To suppress the contamination from this pulsar, only the energy range above 30 GeV was taken into account. The gigaelectronvolt emission from the LHAASO J1908+0621 region was estimated by modelling this region with the sources from the 4FGL catalogue plus an additional component of a 0.5° radius centred at the best-fit position of the LHAASO source. The whole energy range from 30 to 250 GeV was divided in four logarithmically spaced energy bins, and the γ -ray flux in each bin was obtained by a likelihood-based computation. The derived energy fluxes are shown in Extended Data Fig. 5.

Gas distributions. To derive the density of the molecular cloud in the vicinity of LHAASO 1908+0621, we use the CO survey data from ref. ³². We integrate the velocity range of 48–54 km s⁻¹, which corresponds to a distance of 3 kpc. We find significant CO emission towards PSR J1907+0602 and the supernova remnant SNR G40.5-0.5. The maximum of the KM2A significance map is between these two objects, where we also find some dense filaments. We use the standard assumption of a linear relationship between the velocity-integrated brightness temperature of the CO line, W_{CO} , and the column density of molecular hydrogen, $N(\text{H}_2)$, that is, $N(\text{H}_2) = X_{\text{CO}} \times W_{\text{CO}}$. The conversion factor $X_{\text{CO}} = 2.0 \times 10^{20} \text{ cm}^{-2} \text{ K}^{-1} \text{ km}^{-1} \text{ s}$ is adopted. The derived gas mass in the γ -ray emission region is $1.5 \times 10^4 M_\odot$ (M_\odot , mass of the Sun), assuming a distance of 2.4 kpc. Thus, the average density is estimated as 10 cm^{-3} .

Modelling leptonic and hadronic γ -ray production in LHAASO J1908+0621. Here we describe the details of phenomenological modelling of γ -rays in LHAASO J1908+0621. In the leptonic scenario, we assume that the injection particle spectrum follows the form

$$Q(E) \equiv \frac{dN}{dE dt} = N_0 E^{-\alpha} \exp[-(E/E_0)^\beta], \quad (1)$$

where α is the power-law index of the injection spectrum, E_0 is the cutoff energy and N_0 is the normalization factor, which is related to the injection luminosity L_{inj} of the particle through

$$L_{\text{inj}} = \int_{E_{\text{min}}}^{\infty} E \frac{dN}{dE dt} dE = \eta_e L_s, \quad (2)$$

where E_{min} is the minimum energy in the electron injection spectrum, L_s is the spindown luminosity of PSR J1907+0602 and η_e is the fraction of the spindown luminosity converted to the electron injection luminosity. In equation (2), we consider that the injection rate history follows the spindown history of the pulsar, assuming a braking index fixed at 2 and an initial rotation period P_0 . β indicates the sharpness of the cutoff. Previous analysis³³ shows that $\beta = 2$ (that is, a super-exponential cutoff) is expected if the Bohm diffusion applies in the particle acceleration region and a $\dot{E} \propto E^2$ type energy loss process is taken into account at the mean time. The time-integrated electron spectrum is influenced by the radiative cooling with a cooling rate

$$\dot{E}_e = -\frac{4}{3} \sigma_T c \left(\frac{E_e}{m_e c^2} \right)^2 \left[U_B + f_{\text{KN}}(E_e) U_{\text{ph}} \right], \quad (3)$$

where σ_T is the Thomson cross-section, U_B and U_{ph} are the magnetic energy density and the radiation energy density, respectively. f_{KN} accounts for the Klein–Nishina effect, and can be approximated by $f_{\text{KN}} = \{1 + [2.82kT_e/(m_e c^2)]^{0.6}\}^{-1.9/0.6}$ for a blackbody-type radiation field of temperature T , with k being the Boltzmann constant. The cooling timescale can be shorter than the age of the system t_{age} at high energies, so the time-integrated spectrum will be influenced by the radiative cooling processes. The spectrum evolution is described by

$$\frac{\partial}{\partial t} \left(\frac{dN}{dE_e} \right) = \frac{\partial}{\partial E_e} \left(\dot{E}_e \frac{dN}{dE_e} \right) + Q(E_e), \quad (4)$$

with solution

$$\frac{dN}{dE_e} = \frac{1}{\dot{E}_e} \int_{E_e}^{E_{\text{eff}}} Q(E'_e, t') dE'_e, \quad (5)$$

where E_{eff} can be calculated from $t_{\text{age}} = \int_{E_e}^{E_{\text{eff}}} dE'_e / \dot{E}_e(E'_e)$ and $t' = \int_{E'_e}^{E_{\text{eff}}} dE''_e / \dot{E}_e(E''_e)$. The inverse Compton spectrum is calculated following the analytical method developed in ref. ³⁴. Parameters α , E_0 , P_0 and η_e are left free in the spectral fitting.

In the hadronic scenario, the proton injection spectrum is assumed to be of the same form as equation (1), except using $\beta = 1$, because the acceleration of the proton is generally limited by the age of the system or escape. The proton injection rate is assumed to be constant. The energy loss timescale of protons through the pp collision is $t_{pp} \approx 5 \times 10^6 [n/(10 \text{ cm}^{-3})]^{-1} \text{ yr}$, which is much longer than the expected age of the system. Thus, the time-integrated proton spectrum should follow the injection spectrum, and is given by

$$\frac{dN}{dE_p} = t_{\text{age}} N_0 E_p^{-\alpha} \exp[-(E_p/E_0)]. \quad (6)$$

We employ the semi-analytical method developed in ref. ³⁵ to calculate the pionic γ -ray spectrum.

Data availability

The data supporting the conclusions of this paper are available through the LHAASO web page (<http://english.ihep.cas.cn/lhaaso/index.html>) in the section ‘Public Data’. All data are in ASCII, and the code used to produce the figures is publicly accessible and listed in the Public Data section.

21. He, H. Design of the LHAASO detectors. *Rad. Det. Technol. Meth.* **2**, 7 (2018).
22. Fleysher, R., Fleysher, L., Nemethy, P. & Mincer, A. I. Tests of statistical significance and background estimation in gamma-ray air shower experiments. *Astrophys. J.* **603**, 355–362 (2004).
23. Bartoli, B. et al. TeV gamma-ray survey of the northern sky using the ARGO-YBJ detector. *Astrophys. J.* **779**, 27 (2013).
24. Cronin, J. W., Gibbs, K. G. & Weekes, T. C. The search for discrete astrophysical sources of energetic gamma radiation. *Annu. Rev. Nucl. Part. Sci.* **43**, 883–925 (1993); erratum **43**, 883–937 (1993).
25. Aharonian, F., Buckley, J., Kifune, T. & Sinnis, G. High energy astrophysics with ground-based gamma ray detectors. *Rep. Prog. Phys.* **71**, 096901 (2008).
26. Aharonian, F. et al. The Crab nebula and pulsar between 500 GeV and 80 TeV: observations with the HEGRA stereoscopic air Cerenkov telescopes. *Astrophys. J.* **614**, 897–913 (2004).
27. MAGIC Collaboration. MAGIC very large zenith angle observations of the Crab Nebula up to 100 TeV. *Astron. Astrophys.* **635**, A158 (2020).
28. Gould, R. J. & Schröder, G. Opacity of the Universe to high-energy photons. *Phys. Rev. Lett.* **16**, 252–254 (1966).
29. Popescu, C. C. et al. A radiation transfer model for the Milky Way: I. Radiation fields and application to high-energy astrophysics. *Mon. Not. R. Astron. Soc.* **470**, 2539–2558 (2017).
30. Moskalenko, I. V., Porter, T. A. & Strong, A. W. Attenuation of very high energy gamma rays by the Milky Way interstellar radiation field. *Astrophys. J. Lett.* **640**, L155–L158 (2006).
31. Abdollahi, S. et al. Fermi Large Area Telescope fourth source catalog. *Astrophys. J. Suppl. Ser.* **247**, 33 (2020).
32. Dame, T. M., Hartmann, D. & Thaddeus, P. The Milky Way in molecular clouds: a new complete CO survey. *Astrophys. J.* **547**, 792–813 (2001).
33. Zirakashvili, V. N. & Aharonian, F. Analytical solutions for energy spectra of electrons accelerated by nonrelativistic shock-waves in shell type supernova remnants. *Astron. Astrophys.* **465**, 695–702 (2007).
34. Khangulyan, D., Aharonian, F. A. & Kelner, S. R. Simple analytical approximations for treatment of inverse Compton scattering of relativistic electrons in the blackbody radiation field. *Astrophys. J.* **783**, 100 (2014).
35. Kafexhiu, E., Aharonian, F., Taylor, A. M. & Vila, G. S. Parametrization of gamma-ray production cross sections for p p interactions in a broad proton energy range from the kinematic threshold to PeV energies. *Phys. Rev. D* **90**, 123014 (2014).
36. Manchester, R. N., Hobbs, G. B., Teoh, A. & Hobbs, M. The Australia Telescope National Facility pulsar catalogue. *Astron. J.* **129**, 1993–2006 (2005).
37. Shan, S. S. et al. Distances of Galactic supernova remnants using red clump stars. *Astrophys. J. S* **238**, 35 (2018).
38. Acero, F. et al. Constraints on the Galactic population of TeV pulsar wind nebulae using Fermi Large Area Telescope observations. *Astrophys. J.* **773**, 77 (2013).
39. Ranasinghe, S. & Leahy, D. A. Distances to supernova remnants G20.4 + 0.1, G24.7 – 0.6, and G28.6 – 0.1 and new molecular cloud associations. *Mon. Not. R. Astron. Soc.* **477**, 2243–2250 (2018).
40. Gotthelf, E. V., Halpern, J. P., Terrier, R. & Mattana, F. Discovery of an energetic 38.5 ms pulsar powering the gamma-ray source IGR J18490-0000/HESS J1849-000. *Astrophys. J. Lett.* **729**, L16 (2011).
41. Zhang, B. et al. The parallax of W43: a massive star-forming complex near the Galactic bar. *Astrophys. J.* **781**, 89 (2014).
42. Yang, J., Zhang, J.-L., Cai, Z.-Y., Lu, D.-R. & Tan, Y.-H. Molecular gas distribution around the supernova remnant G40.5 0.5. *Chin. J. Astron. Astrophys.* **6**, 210–216 (2006).
43. Downes, A. J. B., Pauls, T. & Salter, C. J. G 40.5-0.5: a previously unrecognised supernova remnant in Aquila. *Astron. Astrophys.* **92**, 47–50 (1980).
44. Gelfand, J. D., Slane, P. O. & Temim, T. The properties of the progenitor supernova, pulsar wind, and neutron star inside PWN G54.1+0.3. *Astrophys. J.* **807**, 30 (2015).

Article

45. Kirichenko, A. et al. Optical observations of PSR J2021+3651 in the Dragonfly nebula with the GTC. *Astrophys. J.* **802**, 17 (2015).
46. Azimlu, M. & Fich, M. Study of molecular clouds associated with H II regions. *Astron. J.* **141**, 123 (2011).
47. Paredes, J. M. et al. Radio continuum and near-infrared study of the MGRO J2019+37 region. *Astron. Astrophys.* **507**, 241–250 (2009).
48. Bartoli, B. et al. Observation of the TeV gamma-ray source MGRO J1908+06 with ARGO-YBJ. *Astrophys. J.* **760**, 110 (2012).
49. Chaves, R. C. G. et al. The H.E.S.S. Galactic plane survey. *Astron. Astrophys.* **612**, A1 (2018).
50. Rygl, K. L. J. et al. Parallaxes and proper motions of interstellar masers toward the Cygnus X star-forming complex. I. Membership of the Cygnus X region. *Astron. Astrophys.* **539**, A79 (2012).
51. Kothes, R., Uyaniker, B. & Pineault, S. The supernova remnant G106.3+2.7 and its pulsar-wind nebula: relics of triggered star formation in a complex environment. *Astrophys. J.* **560**, 236–243 (2001).

Acknowledgements This work is supported in China by National Key R&D programme of China under grants 2018YFA0404201, 2018YFA0404202, 2018YFA0404203 and 2018YFA0404204 and by NSFC (grant numbers 12022502, 11905227, U1931112, 11635011, 11761141001 and U2031105), and in Thailand by RTA6280002 from Thailand Science Research and Innovation. We thank all staff members who work year-round at the LHAASO site at 4,400 m above sea level to maintain the detector and keep the electricity power supply and other components of the experiment operating smoothly. We are grateful to Chengdu Management Committee of Tianfu New Area for constant financial support to research with LHAASO data.

Author contributions This work is the result of the contributions and efforts of all members and institutes of the LHAASO Collaboration under the leadership of Zhen Cao, who is the spokesperson of the LHAASO collaboration. Most of the listed 32 institutes participate in the construction of the LHAASO detectors. In particular, H.H.H. leads the design and construction of KM2A, whose scintillator detector array is constructed by teams led by X.D.S. and muon detector array is constructed by teams led by G.X. KM2A is operated by teams led by J.L. and X. Zuo. The calibration of LHAASO detectors is led by H.H.H. with the participation of groups from IHEP, led by H.K.L. and X. Zuo; from Shandong University, led by C.F.F.; from the University

of Science and Technology of China, led by C. Li; and from Southwest Jiaotong University, led by H.Y.J. The CR event reconstruction is led by S.Z.C. with the participation of groups from IHEP, Shandong University and Southwest Jiaotong University. The data analysis by groups from IHEP and Shandong University is led by S.Z.C.; from Sun Yat-sen University by P.H.T.T.; and from the University of Science and Technology of China by R.Z.Y. The team at Purple Mt Observatory, led by Yi Zhang, performs an independent cross-check of the analysis. R.Z.Y. and R.Y.L. lead the interpretation of the results, with participation of the groups from Nanjing University, led by Y.C. and X.Y.W.; from Yunnan University, led by L. Zhang; from Purple Mt Observatory, led by Q.Y. Zhen Cao, F.A.A. and B.D.P. supervised the data analysis and interpretation and also lead the paper writing. S.M.L. and D.d.V. contribute as co-chairs of the editorial board of LHAASO. Many groups participated in the analysis procedures, including the groups from Mahidol University, led by D.R.; from Shanghai Jiaotong University, led by H. Zhou; from Shanghai Observatory, led by Z.X.W.; from Peking University, led by Zhuo Li; from Guangxi University, led by E.W.L.; from National Observatory, led by W.W.T.; from Wuhan University, led by P. H. T. Tam; and from Yunnan Observatory, led by J.C.W. All other groups—from the University of Chinese Academy of Science and Tianfu Cosmic ray Research Center, led by Zhen Cao; from State Key Laboratory of Particle Detection and Electronics, led by Q.A.; from Tsinghua University, led by Y.N.L.; from the National Space Science Center, led by Z.B.S.; from Guangzhou University, led by J.H.F.; from Hebei Normal University, led by S.W.C.; from Zhengzhou University, led by H.D.L.; from Sichuan University, led by C.W.Y.; from Tibet University, led by T.L.C.; and from the Institute for Nuclear Research and Moscow Institute of Physics and Technology, led by Yu.V.S.—contributed to detector construction and to reviewing the final version before submission.

Competing interests The authors declare no competing interests.

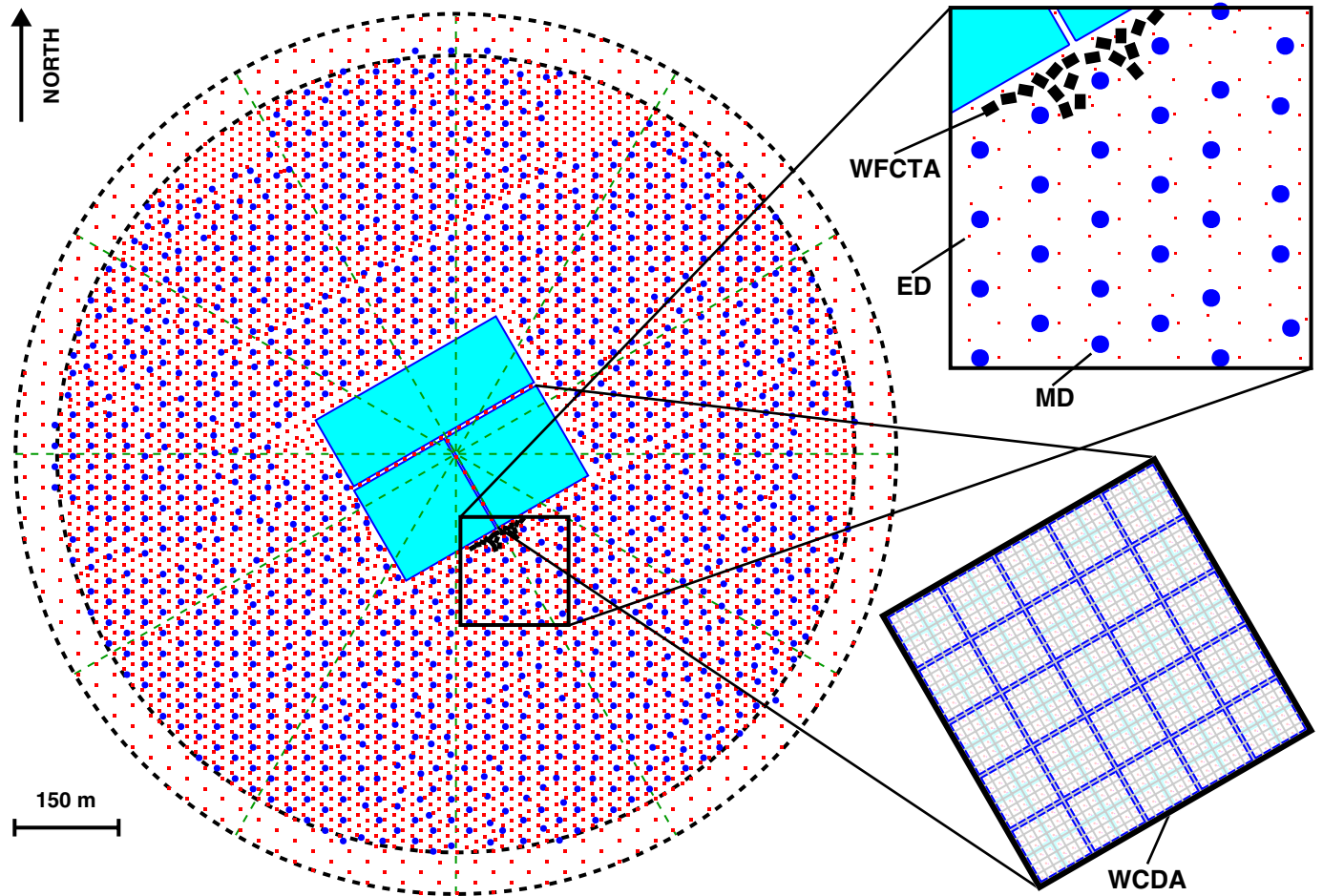
Additional information

Supplementary information The online version contains supplementary material available at <https://doi.org/10.1038/s41586-021-03498-z>.

Correspondence and requests for materials should be addressed to Z.C., F.A.A., S.Z.C., R.Y.L. or R.Z.Y.

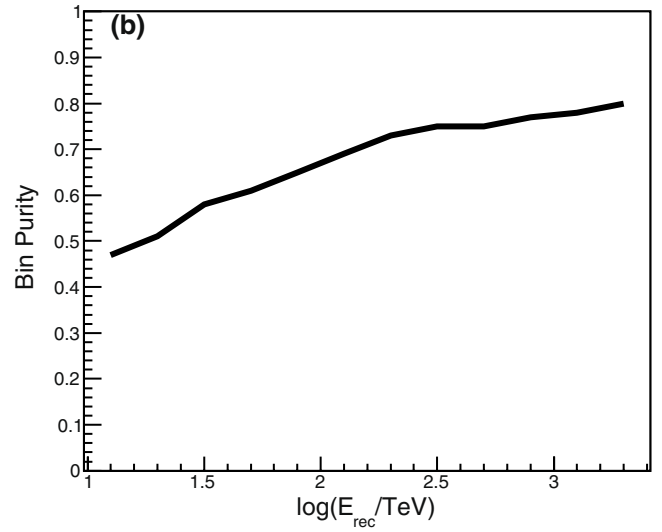
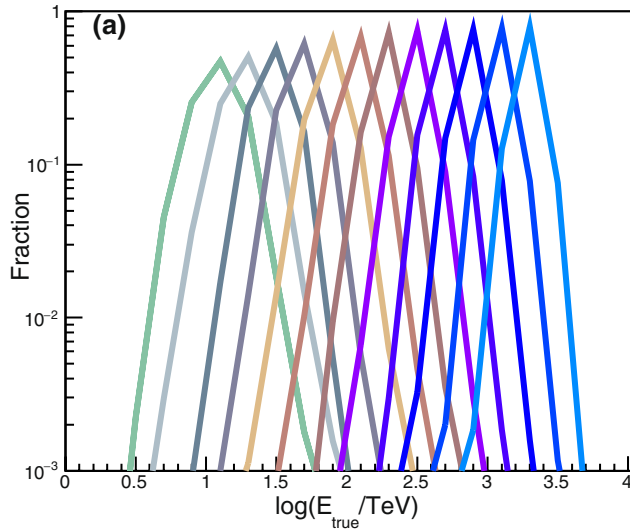
Peer review information *Nature* thanks Razmik Mirzoyan and the other, anonymous, reviewer(s) for their contribution to the peer review of this work. Peer reviewer reports are available.

Reprints and permissions information is available at <http://www.nature.com/reprints>.



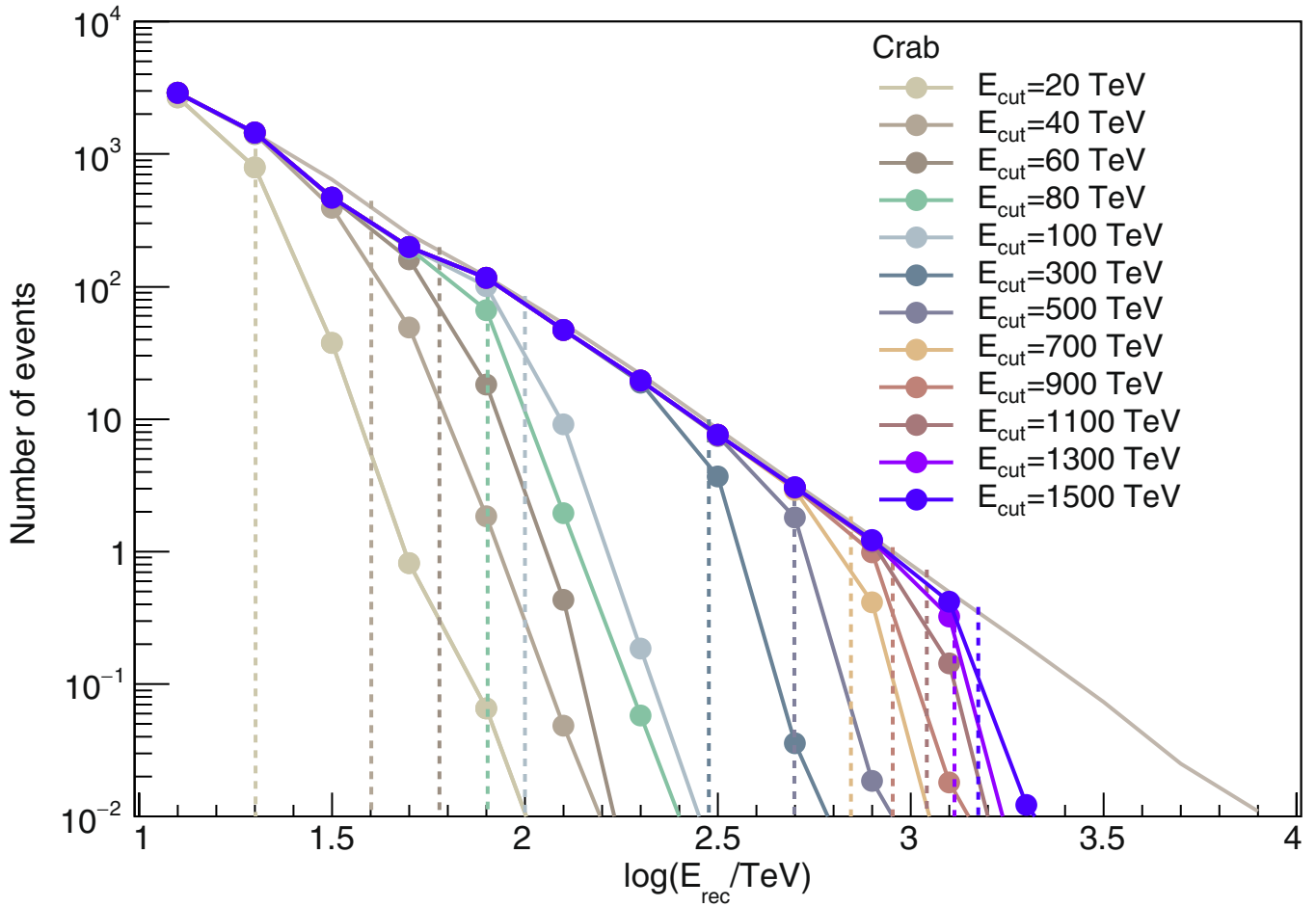
Extended Data Fig. 1 | Schematic drawing of the LHAASO layout⁷. Small red dots indicate the 5,195 scintillator counters, with a spacing of 15 m in the central area of 1 km² and of 30 m in the skirt area of 0.3 km² of KM2A. Big blue dots indicate the 1,188 muon detectors distributed in the central area with a spacing

of 30 m. The three light-blue rectangles in the centre indicate WCDA, of 78,000 m² in total. Small black rectangles near WCDA indicate 18 telescopes of WFCTA.



Extended Data Fig. 2 | γ -ray energy distributions in SED bins and corresponding bin purity. **a**, Distributions of thrown-in energies E_{true} in the simulation of events that are in the bins, defined by reconstructed energies E_{rec} above 10 TeV. The fraction on the vertical axis is defined as $(dN/dE_{\text{true}})/N_i$, where N_i is the total number of events in the i th bin, defined by the reconstructed

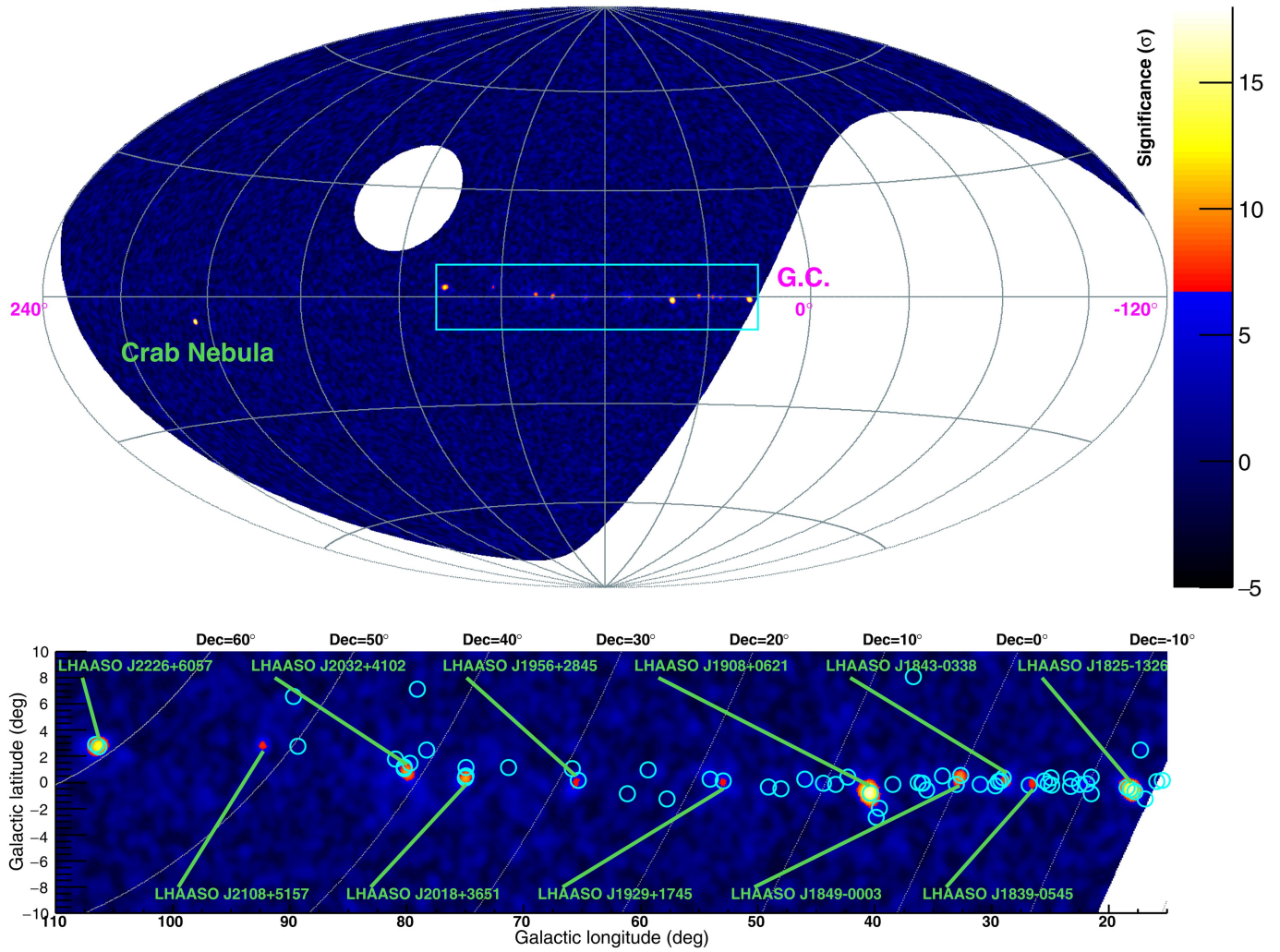
energy E_{rec} . A bin width of $\Delta(\log E_{\text{rec}}) = 0.2$ is selected, according to the energy resolution of 14% above 100 TeV (ref. ⁸). A power-law spectrum proportional to $E^{-3.09}$ is assumed here. **b**, Bin purity, defined as the fraction of events with E_{true} in the bin, as a function of E_{rec} in the range from 10 TeV to 2.5 PeV.



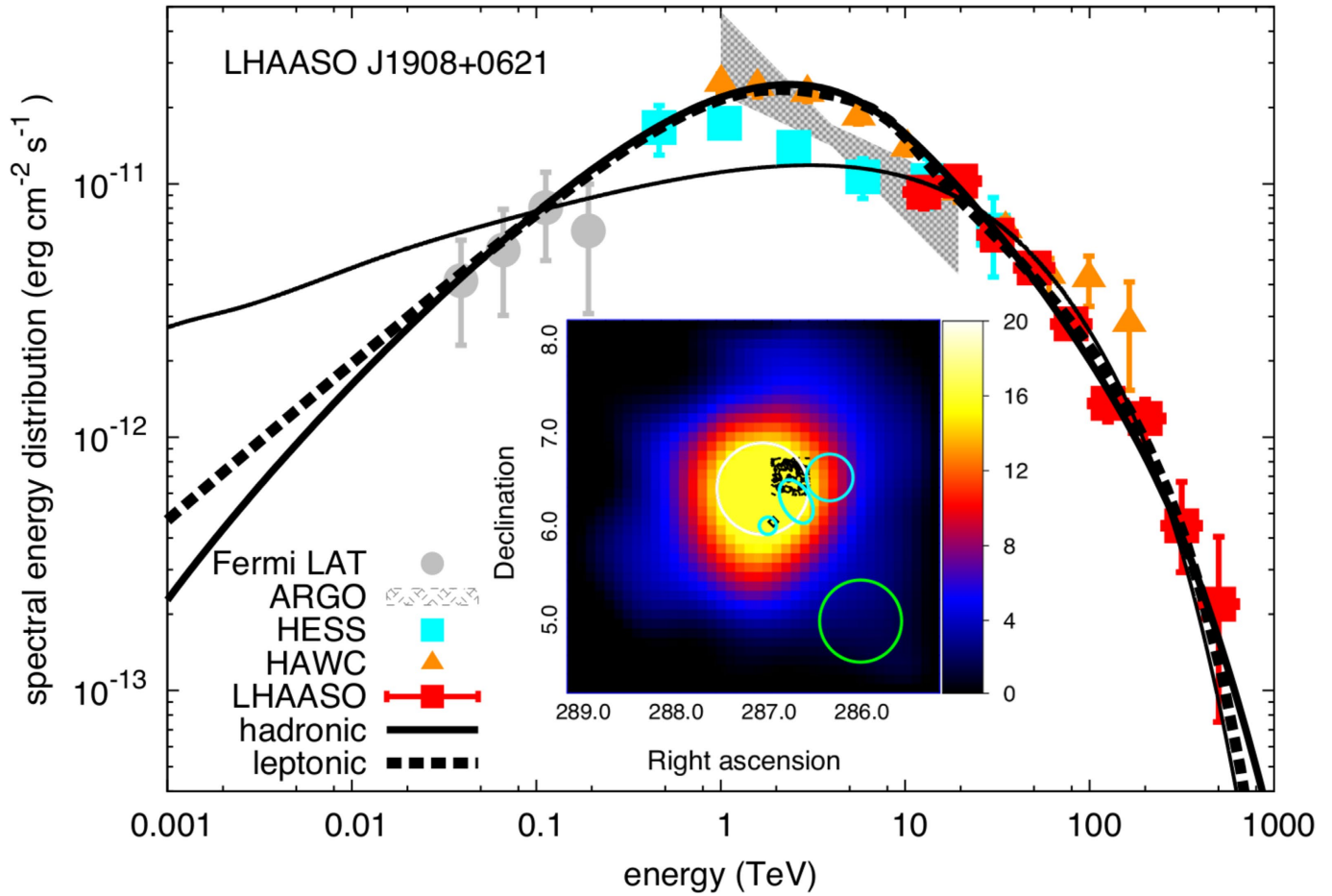
Extended Data Fig. 3 | Distributions (dots) of events in the reconstructed energy bins from 10 TeV to 10 PeV. The input (solid grey line) events are generated using the power-law SED determined from the measured SED of the Crab Nebula⁸. For each case, the input SED has an artificial cutoff (dashed lines)

at the E_{cut} values listed in the key. The distributions demonstrate a clear spillover effect by the events in the bins above E_{cut} . The effect becomes weaker at higher energies. There is no indication of pollution of the bins above 1 PeV by events at input energies lower than 0.3 PeV.

LHAASO Sky @ >100 TeV



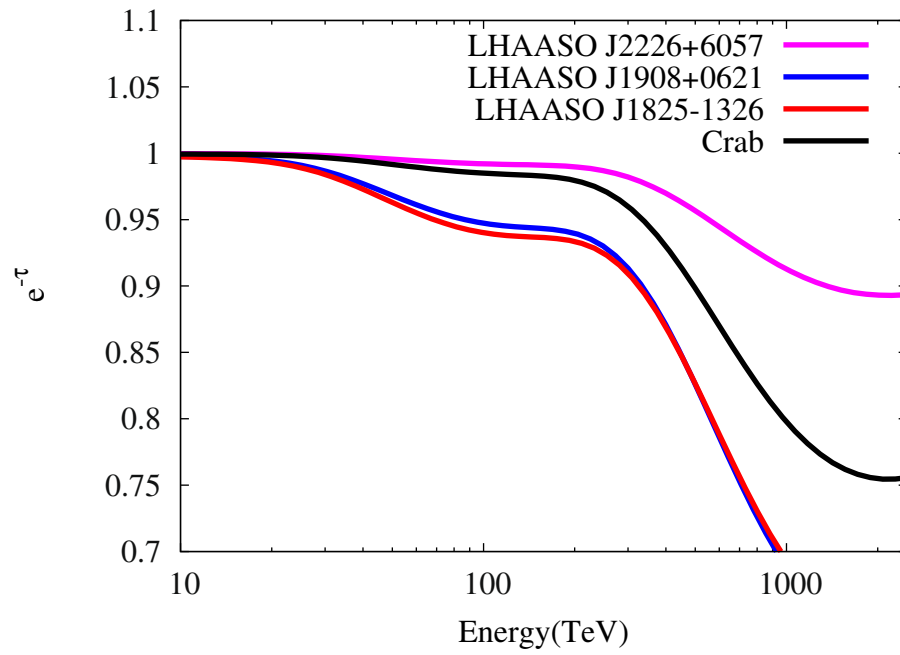
Extended Data Fig. 4 | LHAASO sky map at energies above 100 TeV. The circles indicate the positions of known very-high-energy γ -ray sources.



Extended Data Fig. 5 | Phenomenological fits to the γ -ray observations of LHAASO J1908+0621, and previous observations of potential counterparts.

The inset shows the KM2A significance map, indicating the potential counterparts of the UHE γ -ray source. The colour bar shows the significance (\sqrt{TS}). The green circle indicates the PSF of LHAASO. The Fermi LAT points for LHAASO J1908+0621 analysed in this work, as well as ARGO⁴⁸, HESS⁴⁹ and HAWC⁴ data, are shown together with the LHAASO measurements. The dotted curve shows the leptonic model of radiation, assuming an injection of electron/positron pairs according to the pulsar's spin-down behaviour, with a breaking index of 2 and an initial rotation period of 0.04 s. A fraction of 6% of the current spin-down power of the pulsar PSR J1907+0602 at a distance of 2.4 kpc is assumed to be converted to e^\pm pairs to support the γ -ray emission. The injection spectrum of electrons is assumed to be $N(E) \propto E_e^{-1.75} \exp\{-[E_e/(800 \text{ TeV})]^2\}$.

The solid curves correspond to the hadronic model of radiation. Two types of energy distributions are assumed for the parent proton population: (i) a single power-law spectrum of parent protons, $N(E) \approx E^{-1.85} \exp[-E/(380 \text{ TeV})]$ (thin solid curve); (ii) a broken power-law spectrum with an exponential cutoff of parent protons, with indices 1.2 and 2.7 below and above 25 TeV, respectively, and a cutoff energy of 1.3 PeV (thick solid curve). In the inset sky map, the black diamond shows the position of PSR J1907+0602, the black contours correspond to the location of supernova remnant SNR G40.5-0.5 and the white circle is the position and size of HESS J1908+063. The cyan regions are the dense clumps described in Methods. The average density in the whole γ -ray emission region is estimated to be about 10 cm^{-3} . γ -ray absorption due to photon-photon pair production (see Methods) is taken into account in the theoretical curve.



Extended Data Fig. 6 | γ -ray opacity of LHAASO J2226+6057, J1908+0621, J1825-1326 and Crab Nebula. The absorption due to both ISRFs and CMB is taken into account.

Extended Data Table 1 | Number of on-source events of energy >100 TeV, residual CR background events and corresponding exposure time for the 12 UHE sources

source	Number of on-source events	number of background events	exposure (hr)
LHAASO J0534+2202	67	5.5	2236.4
LHAASO J1825-1326	61	3.2	1149.3
LHAASO J1839-0545	26	4.2	1614.5
LHAASO J1843-0338	30	4.3	1715.4
LHAASO J1849-0003	36	4.8	1865.3
LHAASO J1908+0621	74	5.1	2058.0
LHAASO J1929+1745	29	5.8	2282.6
LHAASO J1956+2845	34	6.1	2461.5
LHAASO J2018+3651	42	6.3	2610.7
LHAASO J2032+4102	45	6.7	2648.2
LHAASO J2108+5157	30	6.4	2525.8
LHAASO J2226+6057	60	6.2	2401.3

Article

Extended Data Table 2 | List of energetic astrophysical objects possibly associated with each LHAASO source

LHAASO Source	Possible Origin	Type	Distance (kpc)	Age (kyr) ^a	L_s (erg/s) ^b	Potential TeV Counterpart ^c
LHAASO J0534+2202	PSR J0534+2200	PSR	2.0	1.26	4.5×10^{38}	Crab, Crab Nebula
LHAASO J1825-1326	PSR J1826-1334	PSR	3.1 ± 0.2^d	21.4	2.8×10^{36}	HESS J1825-137, HESS J1826-130, 2HWC J1825-134
	PSR J1826-1256	PSR	1.6	14.4	3.6×10^{36}	
LHAASO J1839-0545	PSR J1837-0604	PSR	4.8	33.8	2.0×10^{36}	2HWC J1837-065, HESS J1837-069, HESS J1841-055
	PSR J1838-0537	PSR	1.3^e	4.9	6.0×10^{36}	
LHAASO J1843-0338	SNR G28.6-0.1	SNR	9.6 ± 0.3^f	$< 2^f$	—	HESS J1843-033, HESS J1844-030, 2HWC J1844-032
LHAASO J1849-0003	PSR J1849-0001	PSR	7^g	43.1	9.8×10^{36}	HESS J1849-000, 2HWC J1849+001
	W43	YMC	5.5^h	—	—	
LHAASO J1908+0621	SNR G40.5-0.5	SNR	3.4^i	$\sim 10 - 20^j$	—	MGRO J1908+06, HESS J1908+063, ARGO J1907+0627, VER J1907+062, 2HWC 1908+063
	PSR 1907+0602	PSR	2.4	19.5	2.8×10^{36}	
	PSR 1907+0631	PSR	3.4	11.3	5.3×10^{35}	
LHAASO J1929+1745	PSR J1928+1746	PSR	4.6	82.6	1.6×10^{36}	2HWC J1928+177, 2HWC J1930+188, HESS J1930+188, VER J1930+188
	PSR J1930+1852	PSR	6.2	2.9	1.2×10^{37}	
	SNR G54.1+0.3	SNR	$6.3^{+0.8}_{-0.7}^d$	$1.8 - 3.3^k$	—	
LHAASO J1956+2845	PSR J1958+2846	PSR	2.0	21.7	3.4×10^{35}	2HWC J1955+285
	SNR G66.0-0.0	SNR	2.3 ± 0.2^d	—	—	
LHAASO J2018+3651	PSR J2021+3651	PSR	$1.8^{+1.7}_{-1.4}^l$	17.2	3.4×10^{36}	MGRO J2019+37, VER J2019+368, VER J2016+371
	Sh 2-104	H II/YMC	$3.3 \pm 0.3^m/4.0 \pm 0.5^n$	—	—	
LHAASO J2032+4102	Cygnus OB2	YMC	1.40 ± 0.08^o	—	—	TeV J2032+4130, ARGO J2031+4157, MGRO J2031+41, 2HWC J2031+415, VER J2032+414
	PSR 2032+4127	PSR	1.40 ± 0.08^o	201	1.5×10^{35}	
	SNR G79.8+1.2	SNR candidate	—	—	—	
LHAASO J2108+5157	—	—	—	—	—	—
LHAASO J2226+6057	SNR G106.3+2.7	SNR	0.8^p	$\sim 10^p$	—	VER J2227+608, Boomerang Nebula
	PSR J2229+6114	PSR	0.8^p	$\sim 10^p$	2.2×10^{37}	

The properties of pulsars are retrieved from the ATNF pulsar catalogue³⁶ or as specified.

^aCharacteristic age of pulsars.

^bPresent spindown luminosity of pulsars.

^cNearby teraelectronvolt sources within 1° of the centre of the LHAASO source, according to <http://tevcat.uchicago.edu/> (ref. ³⁶).

^dFrom ref. ³⁷.

^eFrom ref. ³⁸.

^fFrom ref. ³⁹.

^gFrom ref. ⁴⁰.

^hFrom ref. ⁴¹.

ⁱFrom ref. ⁴².

^jFrom ref. ⁴³.

^kFrom ref. ⁴⁴.

^lFrom ref. ⁴⁵.

^mFrom ref. ⁴⁶.

ⁿFrom ref. ⁴⁷.

^oFrom ref. ⁵⁰.

^pFrom ref. ⁵¹.